Geophys. J. Int. (1998) **133**, 529–540

Anisotropy in the Indian Ocean upper mantle from Rayleigh- and Love-waveform inversion

J. J. Lévêque,[1] E. Debayle[2] and V. Maupin[3]

[1] *Institut de Physique du Globe (CNRS and Université Louis Pasteur), 5 rue René Descartes, 67084 Strasbourg Cedex, France*
[2] *Research School of Earth Sciences, Australian National University, Canberra, Australia*
[3] *Department of Geophysics, University of Oslo, Norway*

Accepted 1997 November 10. Received 1997 October 30; in original form 1997 April 14.

SUMMARY

A tomographic method is applied to Love- and Rayleigh-wave seismograms in order to address the problem of upper-mantle elastic anisotropy in the Indian Ocean. The first step in our approach is a waveform inversion: for each path of the study, a 1-D depth-dependent model compatible with the waveforms of the fundamental mode and several higher modes of Love and Rayleigh waves is obtained. Then, the models related to the different paths are inverted in order to retrieve 3-D velocity heterogeneities and anisotropy.

In this paper, both the radial anisotropy and the azimuthal anisotropy of *S* waves are investigated in detail. We find a significant radial anisotropy in the uppermost 300 km of the mantle with an overall amplitude smaller than what is found in global studies. Azimuthal *S*-wave anisotropy is also present. The directions of fast *S*-velocities show rather simple patterns from 100 to 300 km depth, and strong correlations with the direction of absolute plate motion (APM) are found. In the uppermost 100 km, the pattern of fast-velocity directions is complex and does not correlate simply with plate motions. From 100 to 200 km depth, a correlation with APM is found in most oceanic regions. The main lack of correlation is located in the vicinity of La Réunion and Mauritius islands. In this region, the anisotropy exhibits a complex pattern between 100 and 150 km, possibly due to a disturbing effect of the hotspot. At 200 km depth and deeper, azimuthal anisotropy vanishes progressively beneath most of the oceanic regions. No significant azimuthal anisotropy is found beyond 300 km depth.

The depth extent of both azimuthal and radial anisotropy, the amplitude of radial anisotropy and the pattern of azimuthal anisotropy support the idea of a preferential orientation of olivine crystals in a low-viscosity zone beneath the lithosphere. This region would be located between 100 and 200 km in oceanic areas, and possibly deeper, between 200 and 300 km, in continental areas, not well resolved in this study.

Key words: anisotropy, Indian Ocean, surface waves, tomography, upper mantle, waveform analysis.

1 INTRODUCTION

Two effects of seismic anisotropy are commonly observed in the upper mantle beneath oceans. The first one, often called polarization anisotropy or radial anisotropy, is generally invoked to explain the discrepancy between observed Love- and Rayleigh-wave velocities (Aki & Kaminuma 1963; Anderson 1966). The second one is a dependence of velocity on the azimuth of wave propagation. This azimuthal anisotropy was first observed by Forsyth (1975) in surface-wave phase-velocity data for the Pacific Ocean. More recent studies have confirmed that azimuthal anisotropy of surface-wave velocities is present in most oceanic regions: the Indian Ocean (Montagner 1986; Roult, Rouland & Montagner 1987; Montagner & Jobert 1988), the Pacific Ocean (Nishimura & Forsyth 1989) and, more generally, on a global scale (Tanimoto & Anderson 1984, 1985; Montagner & Tanimoto 1990, 1991). A phenomenon commonly proposed to explain seismic anisotropy beneath oceans is the preferential orientation of crystals of olivine, a highly anisotropic mineral abundant in the upper mantle, in the horizontal direction of plate motion. This oriented-olivine model has strong support since it allows one to explain P_n velocity variations with azimuth, *SKS*-wave splitting and both azimuthal and radial anisotropy of surface waves

(e.g. Kawasaki & Konno'o 1984). Moreover, many pieces of evidence for olivine orientation in upper-mantle fabrics have been observed (e.g. Peselnick & Nicolas 1978; Christensen & Salisbury 1979).

In a previous paper (Debayle & Lévêque 1997, hereafter referred to as Paper I), we presented a 3-D *S*-velocity model for the Indian Ocean obtained from long-period Love- and Rayleigh-wave seismograms. In the present paper, we refine our modelling of the upper-mantle structure beneath the Indian Ocean using the same method and the same data set as in Paper I, but now focusing our investigations on the anisotropy of *S* waves. Few studies have used both radial and azimuthal surface-wave anisotropy to constrain the upper-mantle structure. While, from a theoretical point of view, the azimuthal dependence of Rayleigh- and Love-wave phase velocities is a well-established property of a general, slightly anisotropic medium (Smith & Dahlen 1973), azimuthal terms have been shown more recently to be useful to retrieve the depth variation of elastic coefficients (Montagner & Nataf 1986; Tanimoto 1986a). In the formalisms of the latter two papers, the phase velocity of surface waves is written as a sum of azimuthal and non-azimuthal terms. The non-azimuthal terms depend on the five elastic coefficients involved in a transversely isotropic medium with a vertical axis of symmetry, corresponding to the observation of polarization anisotropy. The azimuthal terms depend on eight other combinations of elastic coefficients and are related to the azimuthal variations of surface-wave velocities. These theoretical tools have been used in a few studies of the oceanic upper mantle beneath the Indian and Pacific oceans. For the Indian Ocean, Montagner & Jobert (1988) inverted phase-velocity data for both radial and azimuthal anisotropic coefficients. For the Pacific Ocean, Nishimura & Forsyth (1989) also inverted both polarization and azimuthal anisotropy, using a parametrization that allows one to estimate how far the data are compatible with different reference frames.

In this paper, we present new results on elastic anisotropy beneath the Indian Ocean derived from a waveform inversion technique. As in Paper I, we benefit from an enhanced depth resolution due to the modelling of higher-mode waveforms and from a more homogeneous path coverage, increasing the lateral resolution of anisotropy as compared to previous studies in the same region. We also give, in Appendix A, an interpretation of the two most important combinations of elastic coefficients, related to the *S*-velocity azimuthal anisotropy.

2 METHODOLOGY AND DATA PROCESSING

Most previous tomographic studies involving surface waves and taking into account the effect of anisotropy have been based on the inversion of phase (or group) velocities in a two-step scheme. First, maps of the phase velocities of Love and Rayleigh waves and their azimuthal variations are produced. Then, in a second step, these maps are inverted into 3-D models of the elastic parameters (Montagner & Jobert 1988; Hadiouche, Jobert & Montagner 1989; Nishimura & Forsyth 1989; Montagner & Tanimoto 1991). In contrast to these studies, we perform the inversion using an alternative two-step procedure, in which the phase velocities do not appear directly. The first step is a waveform inversion. It yields a 1-D model, a function of depth, which can be considered as the average

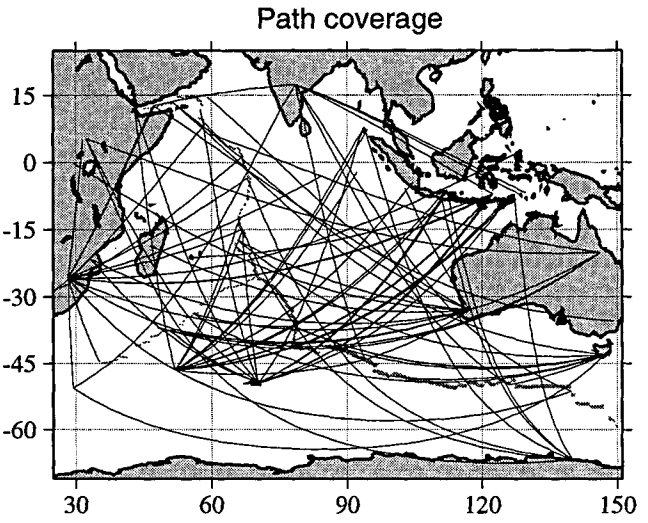

Figure 1. Map of the region under study, and path coverage.

of the Earth's structure beneath the source–receiver great-circle path. The second step is a tomographic inversion of these path-averaged models into a 3-D model of the structure.

The waveform technique is an extension of the method of Cara & Lévêque (1987), adapted to process simultaneously a set of seismograms with close epicentres, recorded at a single station (see Paper I). The path-averaged, 1-D model is designed to fit simultaneously all the seismograms related to the same path, from the cluster of epicentres to the station. The waveform technique gives us the possibility of retrieving information contained in the higher-mode wave trains, thus improving the depth resolution of the model (Cara & Lévêque 1987; Nolet 1990; Lévêque, Cara & Rouland 1991).

As in Paper I, the data set consists of 156 long-period seismograms recorded at broad-band stations in the Indian Ocean, corresponding to 71 paths. For each path, we process at least one Rayleigh- and one Love-wave seismogram in the period range between 20 and 200 s. The path coverage is shown in Fig. 1. We set the *a priori* information in the waveform inversion as in Paper I. Full details about the data and method can also be found in Debayle (1996).

3 PARAMETRIZATION IN THE WAVEFORM INVERSION

Let us first examine how the average source–station 1-D models retrieved in the waveform inversion should be parametrized in terms of elastic coefficients. The waveforms of the surface wave trains depend in a very non-linear way on the elastic parameters. In order to reduce this non-linearity, the inversion is made using secondary observables of the waveforms (Cara & Lévêque 1987). The partial derivatives of these secondary observables with respect to the elastic parameters are linear combinations of the partial derivatives of the phase velocities. We can therefore analyse how the different elastic parameters influence the secondary observables by examining how they affect the phase velocities in anisotropic structures. The first-order variation of the phase velocity as a function of the azimuth of propagation is given in, for example, Montagner & Nataf (1986) and Tanimoto (1986a) for flat structures, and equivalent formulae are given in Tanimoto (1986b) for spherical

structures. Omitting variations in density, the phase velocity of Rayleigh waves propagating in a flat structure in a given azimuth θ depends only on four combinations of the elastic parameters via four different partial derivatives. Using the notation of Montagner & Nataf (1986), we can write

$$\delta C_R = \frac{\partial C_R}{\partial A}(\delta A + B_C \cos 2\theta + B_S \sin 2\theta + C_C \cos 4\theta + C_S \sin 4\theta) + \frac{\partial C_R}{\partial C}\delta C + \frac{\partial C_R}{\partial F}(\delta F + H_C \cos 2\theta + H_S \sin 2\theta) + \frac{\partial C_R}{\partial L}(\delta L + G_C \cos 2\theta + G_S \sin 2\theta). \quad (1)$$

Each combination contains a transverse isotropy term (A, C, F or L) and, in all cases but one, an azimuthal anisotropy term. Similarly, Love-wave phase velocities depend only on two combinations of elastic parameters, related to two different partial derivatives:

$$\delta C_L = \frac{\partial C_L}{\partial L}(\delta L - G_C \cos 2\theta - G_S \sin 2\theta) + \frac{\partial C_L}{\partial N}(\delta N - C_C \cos 4\theta - C_S \sin 4\theta). \quad (2)$$

Not all of these six combinations can be resolved as a function of depth with surface-wave information only. Two approaches may be chosen to circumvent the lack of resolution. *A priori* information, such as petrological constraints, may be used to tie together the variations of different parameters, or one may choose to invert only for the parameters having the largest influence on the data, that is, those having the largest partial derivatives. We choose this latter alternative. Both procedures have been used in the literature (Nataf, Nakanishi & Anderson 1984; Montagner & Jobert 1988; Nishimura & Forsyth 1989; Montagner & Tanimoto 1991; Maupin & Cara 1992). Nishimura & Forsyth (1989) showed that even when using *a priori* information to couple the parameter variations, only the two best-resolved parameters can be interpreted with reasonable confidence, and that for these parameters, the conclusions are similar whether one uses coupling or inverts for all parameters without coupling.

Among the six partial derivatives appearing in the above equations, the two clearly dominant ones are (Montagner & Nataf 1986) $\partial C_R/\partial L$, related to Rayleigh-wave phase velocities, and $\partial C_L/\partial N$, related to Love waves. From eqs (1) and (2), the two combinations of elastic parameters best resolved by surface waves are therefore $\delta\hat{L} = \delta L + G_C \cos 2\theta + G_S \sin 2\theta$ and $\delta\hat{N} = \delta N - C_C \cos 4\theta - C_S \sin 4\theta$. We show in Appendix A that these two combinations of elastic parameters are actually those controlling, in the long-period approximation, the velocities of SV and SH waves propagating horizontally in the azimuth θ. This confirms that even in fully anisotropic structures, the velocity of horizontally propagating SV and SH waves, in a depth range controlled by the period and the rank of the mode, is the most influential factor in the first-order variation of surface-wave phase velocities.

For the inversion to yield directly a parameter describing the degree of anisotropy in the structure, we prefer to use, instead of $\hat{L}$ and $\hat{N}$, a parametrization of the model similar to that used by Takeuchi & Saito (1972). Here we define

$$\hat{\beta}_V = \sqrt{\frac{\hat{L}}{\rho}} = \sqrt{\frac{L + G_C \cos 2\theta + G_S \sin 2\theta}{\rho}},$$
$$\hat{\xi} = \frac{\hat{N}}{\hat{L}} = \frac{N - C_C \cos 4\theta - C_S \sin 4\theta}{L + G_C \cos 2\theta + G_S \sin 2\theta}. \quad (3)$$

Their partial derivatives are the partial derivatives $\partial C/\partial\beta_V$ and $\partial C/\partial\xi$ of a transversely isotropic structure with a vertical axis of symmetry.

In the absence of azimuthal anisotropy (or if the azimuthal variation has been averaged out), these parameters reduce to β_V and ξ as defined by Takeuchi & Saito (1972). In the presence of azimuthal anisotropy, they are the apparent β_V and ξ parameters resolved by surface waves propagating in the azimuth θ. The advantage of using $\hat{\xi}$ directly in the inversion, compared to inverting for $\hat{L}$ and $\hat{N}$ and calculating afterwards the ratio $\hat{N}/\hat{L}$, is that we avoid the inconsistencies which arise from comparing models at differing resolution. However, choosing $\hat{\xi}$ has a disadvantage in terms of azimuthal variations: this parameter experiences both 2θ and 4θ variations, while $\hat{L}$ varies with 2θ only and $\hat{N}$ with 4θ only. As we will see later on, the azimuthal variation of $\hat{\xi}$ cannot be resolved in our study and its more complex azimuthal behaviour is no disadvantage in our case.

The above discussion has been worked out in the framework of flat earth structures. For studies on the regional scale (a few thousand kilometres in the Indian Ocean), the Earth's sphericity cannot be neglected. For spherical structures, Tanimoto (1986b) and Mochizuki (1986) showed that the expressions for the velocity perturbation in spherical anisotropic structures tend to the corresponding expressions for flat structures at short periods, and we can expect eqs (1) and (2) to remain a good approximation in our case. In this study, we use partial derivatives calculated for spherical structures (Takeuchi & Saito 1972). We do neglect the three partial derivatives related to the elastic parameters A, C and F, but we keep in the inversion the partial derivatives $\partial C_R/\partial N$ and $\partial C_L/\partial L$, in addition to the dominant ones $\partial C_R/\partial L$ and $\partial C_L/\partial N$. These additional partial derivatives are small. Indeed, $\partial C_R/\partial N$ is exactly zero in flat structures and, even if it takes non-zero values in a spherical structure, it is always much smaller than $\partial C_R/\partial L$. On the other hand, $\partial C_L/\partial L$ is non-null in flat as well as in spherical structures, but it is always smaller than $\partial C_L/\partial N$. A consequence of this choice is that the azimuthal variations contained in our inverted parameters $\tilde{\beta}_V$ and $\tilde{\xi}$ are not strictly those of $\hat{\beta}_V$ and $\hat{\xi}$ as defined in eq. (3), but are so close that they can be interpreted as such.

4 FROM PATH-AVERAGED MODELS TO THE 3-D MODEL

Applying the waveform inversion to our data set for the Indian Ocean, we get for each path i the two depth-dependent models $\hat{\beta}_i(z)$ and $\hat{\xi}_i(z)$. We can then combine these path-averaged models into one single 3-D model for the Indian Ocean via a tomographic inversion. Actually, this inversion is performed depth by depth. In order to analyse the results of the tomographic inversion, we compute at each depth the quality criterion

$$\chi = \sqrt{\frac{1}{n}\sum_i \left(\frac{\hat{d}_i - d_{ci}}{\sigma_i}\right)^2}, \quad (4)$$

where n is the number of data points; $\hat{d}_i$ is the data $\hat{\beta}_i$ or $\hat{\xi}_i$ for path i at the appropriate depth; d_{ci} is the calculated data for the inverted model, for path i; and σ_i is the standard error of the data (it corresponds to the *a posteriori* standard deviation computed in the waveform inversion). The value of χ is close to 1 when the average data misfit is close to the average data error bar.

Radial anisotropy: the $\hat{\xi}$ parameter

The $\hat{\xi}_i$ models obtained from the waveform inversions have rather large *a posteriori* standard deviations. This is because the accuracy of the $\hat{\xi}_i$ values is damaged by the larger noise level usually present in the Love-wave data. As a consequence, the data do not allow us to retrieve the azimuthal terms of $\hat{\xi}$ (eq. 3) for the Indian Ocean, nor their lateral variations. A simple 1-D average model, without lateral or azimuthal variations, is sufficient to explain the data corresponding to the paths in Fig. 1 within their average error bars (χ close to or less than 1 at each depth). Since the $\hat{\xi}$ parameter we use in the inversion includes azimuthal terms, we might suspect that azimuthal variations might bias the average ξ model if the azimuthal sampling was uneven. However, we are dealing here with the average model for the whole region under study, and the azimuthal coverage to be considered is the global coverage for the whole map (Fig. 1) considered as a single cell. This global coverage is good enough to average out the possible azimuthal variations, so that the average ξ model is not likely to suffer significant bias. The inverted ξ can then be interpreted as the mean ξ parameter of Takeuchi & Saito (1972) for the Indian Ocean.

The ξ model for the whole Indian Ocean, presented in Fig. 2, reveals a significant polarization anisotropy in the uppermost 250–300 km of the mantle. The amplitude of anisotropy is smaller and the depth extent slightly greater than in the PREM model (Dziewonski & Anderson 1981). It is in better agreement down to 400 km with the results of Montagner & Kennett (1996), who determine a set of global reference models giving an acceptable fit to both body-wave and normal-mode data. However, these authors found models with significant radial anisotropy in the whole upper mantle, while we find ξ values departing from 1 in the upper 400 km only. Moreover, the ξ amplitudes they found in the upper part are twice as large as what we find, suggesting that the polarization anisotropy for the Indian Ocean may be weaker than the world average. We can rule out the idea that we over-constrained the ξ parameter in the inversion, for instance by using too small *a priori* values at the waveform modelling stage, since several tests performed on synthetic data showed the ability to retrieve ξ values twice as large as what we find from actual data.

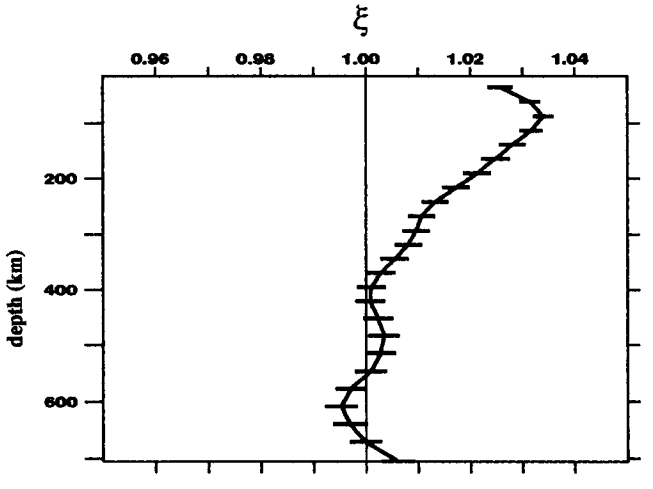

Figure 2. Radial-anisotropy average model obtained for the whole region. Significant anisotropy is observed down to 250–300 km depth.

On the regional scale, Montagner & Jobert (1988) analysed the fundamental mode of Rayleigh and Love waves for the Indian Ocean, and found a significant S-wave radial anisotropy in the whole depth range of their inversion, from 0 to 400 km. Our ξ model indicates a shallower anisotropy, which is more similar to the results of Nishimura & Forsyth (1989) for the Pacific Ocean, who also find anisotropy only in the upper 300–400 km of the mantle, but had no good resolution at greater depths. Our ξ amplitude corresponds to that observed in a 0–4 Ma old basin in the Pacific Ocean, according to these authors. For older oceanic regions of the Pacific Ocean, Nishimura & Forsyth (1989) find larger ξ amplitudes. Again, we find a weaker radial anisotropy for the Indian Ocean than for other oceanic parts of the Earth. The depth of the anisotropic layer in our model can be compared to the results obtained by Cara & Lévêque (1988) for the Pacific Ocean, using higher-mode data, who find significant radial anisotropy in the uppermost 250 km of the mantle for a path crossing the Pacific Ocean. However, comparing the amplitude of anisotropy from this study to that of Cara & Lévêque (1988) is not straightforward, since their ξ model was obtained for a single path in a particular azimuth and is not an azimuthally averaged value.

Velocity and azimuthal anisotropy: the $\hat{\beta}_V$ parameter

The $\hat{\beta}_i$ models are primarily determined by the Rayleigh-wave data. In contrast with the ξ parameter, the precision of the $\hat{\beta}_i$ is such that their azimuthal variations for the Indian Ocean can be resolved. In Paper I, we performed a tomographic inversion of β_V using the continuous regionalization algorithm of Montagner (1986), and obtained maps at different depths of lateral variations of β_V with a lateral resolution of 1000 km. Below 150 km depth, the quality criterion χ is smaller than 1, which means that the data are fitted within their average error bars. On the other hand, in the upper 100 km of the model, lateral variations of β_V do not fully explain the data, since χ is larger than 1, reaching a value of 2.77 at 50 km depth. Part of the residual misfit may be addressed by means of azimuthal anisotropy. In the following sections, we establish and discuss results obtained when allowing for azimuthal anisotropy in the inversion process, in addition to S-velocity heterogeneities and radial anisotropy.

Starting from eq. (3) and omitting variations in density, we can write, at a given depth, the first-order relation

$$\delta\hat{\beta}_V = \delta\beta_V + A_1 \cos 2\theta + A_2 \sin 2\theta, \quad (5)$$

where $\delta\hat{\beta}_V$ is the perturbation of the shear-wave velocity obtained beneath a given path with the waveform inversion, $\delta\beta_V$ is the perturbation of the elastic coefficient β_V, $A_1 = G_C/2\rho\beta_V$, $A_2 = G_S/2\rho\beta_V$ and θ is the azimuth. Parameters $\delta\beta_V$, A_1 and A_2 are retrieved from $\delta\hat{\beta}_V$ using the continuous regionalization algorithm of Montagner (1986). In this algorithm, the *a priori* information on the model is gaussian and is characterized

by two parameters: a horizontal correlation length, which constrains the lateral smoothness of the model, and the *a priori* standard deviation, which controls the allowed variation range of the inverted parameters. The *a priori* values for $\delta\beta_V$ are the same as in Paper I (correlation length = 1000 km and *a priori* standard deviation = 0.1 km s^{-1}). After some trials, we also chose a correlation length of 1000 km for the anisotropic parameters A_1 and A_2, and the *a priori* standard deviation σ_a equal to 0.005 km s^{-1}. This last value may appear very small compared to σ_{β_V}, but it is required to obtain reasonable G amplitudes using the expected values of elastic coefficients in the upper mantle, as estimated by Estey & Douglas (1986). Also, note that this kind of *a priori* information efficiently controls the amplitude but does not impose any constraint on the direction of azimuthal anisotropy.

Even if allowing for azimuthal anisotropy is not sufficient to get χ close to 1 at depths of 50 and 100 km, it is nevertheless a significant improvement since the χ values obtained, 2.14 at 50 km depth and 1.43 at 100 km depth, correspond to variance reductions of 40 per cent and 25 per cent respectively. At larger depths, where the data were already fitted within their error bars, the variance reduction is smaller, decreasing from 14 per cent at 150 km to 8 per cent at 300 km depth.

In Fig. 3 we present the maps obtained of lateral variation of β_V and azimuthal anisotropy. Lateral variations of the elastic coefficient β_V are represented by colours. The A_1 and A_2 values have been transformed into arrows showing the direction of maximum G, which is also the fast direction for SV waves propagating horizontally (see Appendix A). The arrow size is proportional to the percentage of peak-to-peak azimuthal variation of the SV-wave velocity. The error maps for β_V are very similar to those already presented in Paper I.

Allowing for azimuthal anisotropy does not change the velocity maps. This can be checked by comparing Fig. 3 of the present paper with Figs 1 and 2 of Paper I. For example, at 50 km depth, the velocity pattern of Fig. 3(a) is very similar to that of Fig. 1(c) of Paper I, and this holds for the whole depth range of inversion. The trade-off between azimuthal anisotropy and lateral heterogeneities remains weak, and the conclusions of Paper I are unchanged when introducing azimuthal anisotropy into the inversion: the main velocity heterogeneities are confined to the uppermost 250 km of the upper mantle beneath oceans and 300 km beneath continents. The velocity pattern is well correlated with surface tectonics down to 200 km beneath the Indian Ocean, but unexpected short-wavelength anomalies are found, such as high velocities beneath the Carlsberg ridge and, at shallow depth only, beneath the West Indian ridge. We refer the reader to Paper I for a more detailed discussion of β_V maps and we will now focus on the results related to azimuthal anisotropy.

At 50 km depth (Fig. 3a), the pattern of azimuthal anisotropy appears quite complex. The fast directions are perpendicular to the East and Central Indian ridges near the triple junction of Rodriguez but turn clockwise near the island of Amsterdam, to become parallel to the East Indian ridge between 80°E and 100°E, and again perpendicular to the East Indian ridge beyond 100°E. Anisotropy is weak beneath Australia and most continental regions. It is strong below Indonesia and west of 90°E. The maximum peak-to-peak value of the S-wave anisotropy reaches 4.8 per cent beneath the West Indian ridge at 37°E. The average value for the whole map is 1.1 per cent.

At 100 km depth (Fig. 3b), the map displays a simpler pattern of fast direction. Fast directions appear perpendicular to the East and Central Indian ridges along the entire length of these ridges. Conversely, there seems to be no correlation with the direction of the slowly spreading West Indian ridge. The anisotropy beneath Indonesia is now very small, but becomes significant beneath Australia with fast velocities organized in an east–west direction. The average peak-to-peak velocity anisotropy decreases to 0.7 per cent and corresponds to about three times the *a priori* value set for the coefficients A_1 and A_2. The maximum peak-to-peak anisotropy is 2.3 per cent.

At 150 km depth (Fig. 3c), the general pattern of anisotropy is similar to that found at 100 km depth. However, the amount of anisotropy decreases (the average peak-to-peak value is now 0.33 per cent), especially in the western part of the map. The Chagos ridge, Mascareignes plateau and Réunion–Mauritius region display low anisotropy. Azimuthal anisotropy remains large beneath the East Indian ridge and beneath Australia, where the fast directions are still clearly east–west.

At 200 km depth (Fig. 3d), two regions display a large β_V anisotropy with a maximum peak-to-peak value close to 1 per cent: (1) the region between Madagascar and the Central Indian basin displays north–south fast velocities, extending southwards beneath the West Indian ridge and the Rodriguez triple junction as far as 45°S; and (2) a large region where north–south fast-velocity directions appear clearly, which comprises Australia and the southern Indian Ocean near the Australian–Antarctic discordance, and reaches the Antarctic continent. The average peak-to-peak value of β_V anisotropy for the whole map is 0.30 per cent, about the same value as at 150 km depth.

At 300 km depth (Fig. 3f), the azimuthal anisotropy is everywhere very small compared to shallower depths. The two maxima observed on the previous map (south of Madagascar and Australia–Antarctic) are still visible but do not exceed 0.45 per cent. The average peak-to-peak value on the whole map is only 0.15 per cent.

Maps at greater depths (not presented here) display extremely small azimuthal anisotropy, which can be considered as not significant.

5 DISCUSSION

Before discussing the pattern of anisotropy we have obtained for the Indian Ocean upper mantle, we will demonstrate that this pattern is robust. In the previous section, we mentioned that this study of the azimuthal anisotropy was intended to explain part of the misfit remaining after the inversion without azimuthal anisotropy presented in Paper I. However, other phenomena may alternatively explain this residual misfit. Short-wavelength heterogeneities of S velocity are not properly modelled in our inversion, since we use a correlation length of 1000 km. It is well known that sharp lateral transitions exist in the real Earth, such as the ocean–continent boundaries. In the present study, we invert only for the mantle part of the model, after carefully accounting for the average crustal structure along each path. We thus avoid retrieving the sharp crustal boundaries, and are left only with possible sharp mantle transitions. At an early stage of this study, we made attempts to model these sharp mantle transitions by using a pure-path regionalization based on *a priori* boundaries, but we never succeeded in decreasing the misfit with physically acceptable

models. Instead, we decided to perform a regionalization without *a priori* boundaries and we also made attempts to resolve sharp heterogeneities by choosing correlation lengths as small as possible. A value of 500 km allows us to decrease significantly the misfit as compared to 1000 km, but it is an extreme value, at which instabilities in the model perturbations seem to develop already. Conversely, the 1000 km correlation length we finally retained ensures a good stability of the inverted model and allows full coverage of the region under study. This can be seen in Fig. 4, where we represent the model obtained from the inversion of synthetic data corresponding to waves propagating in a laterally homogeneous structure at an S velocity of 6 km s^{-1}, along the same paths as used in this study. The *a priori* model was set equal to 4 km s^{-1}, so that we expect to find a +50 per cent perturbation wherever the combination of the path coverage and the correlation length allows it. It is clear in Fig. 4 that the path coverage and correlation length we have used in this study allow us to recover this flat model uniformly in the whole region. The effect of the correlation length is both to smooth the model perturbation when several paths are available, and to smear the perturbation towards zones not actually sampled by the surface waves. This smearing appears in light blue in Fig. 4 at the edges of the covered area. It can be interpreted as the effect of the width of the gaussian used as the correlation function.

We must also analyse the possible trade-off between azimuthal anisotropy and the short-wavelength heterogeneities that we cannot resolve. If such a trade-off exists, the azimuthal anisotropy we obtain may originate from a mismodelling of heterogeneities. In order to test this, we performed an experiment where synthetic data were computed from the 3-Smac model (Nataf & Ricard 1995) along our paths. We then processed these isotropic synthetic data according to the same scheme as was used for the actual data. The inverted model (Fig. 5) shows a smoothed image of the 3-Smac S velocities and also displays a small amount of azimuthal anisotropy, entirely due to the trade-off between the isotropic part and the anisotropic part of the model, since no anisotropy exists in the 3-Smac model. The azimuthal anisotropy is small on average (0.2 per cent) and shows up mainly in three regions: the easternmost part of Africa and the Somalian basin, the neighbourhood of the Rodriguez triple junction, and the eastern part of the Southeast Indian ridge. While a lack of azimuthal coverage can reasonably be invoked for the first and third regions, it is clearly not the case for the Rodriguez region. The 0.5 per cent peak-to-peak azimuthal anisotropy we obtain in this region is therefore a crude estimate of the trade-off we can expect in our model, if the actual Earth resembles the 3-Smac model. Indeed, the S-velocity contrasts in the 3-Smac model are about 8 per cent, similar to what we find for S velocities at depths greater than 50 km. This 0.5 per cent bias is smaller than the anisotropy we obtain in several regions from real data, down to 250 km depth.

We also performed inversions of the real data, decreasing step by step the correlation length associated with the S-velocity heterogeneities and keeping unchanged the other parameters. If a trade-off exists between short-wavelength heterogeneities and azimuthal anisotropy, it should gradually affect the anisotropy pattern. What we actually find is a great stability of this pattern for correlation lengths between 1000 and 500 km. The overall amplitude of azimuthal anisotropy slightly decreases with the S-velocity correlation length, at all depths except 50 km, where the decrease is more significant. We thus think that our choice of a 1000 km length is conservative with respect to the stability of the anisotropic pattern. We could shorten this correlation length to 500 km without affecting significantly our results. The main changes would be more details, possibly meaningless, in the S-velocity maps and a small reduction of the amplitude of azimuthal anisotropy, but no change in the fast directions of S velocities. Similarly, changing the *a priori* values of parameters A_1 and A_2 results in a change of the amplitude of anisotropy, but does not significantly modify the fast-direction pattern.

A last point we would like to discuss is the ability of our path coverage to resolve azimuthal anisotropy with a 1000 km correlation length. A first piece of the answer comes from the stability of the fast-velocity pattern throughout the various experiments we performed on real data. A second argument is to look at the path coverage (Fig. 1), keeping in mind that we are looking for a 2θ azimuthal variation, which requires sampling each cell in a minimum of only three different directions. It is then clear that our path coverage enables us to retrieve the 2θ azimuthal anisotropy in most of the area under study.

From these experiments, we conclude that trade-off biases between azimuthal anisotropy and S-velocity heterogeneities certainly exist, but remain small in amplitude and very small in direction. We think that the pattern of directions of fast S velocities we find is sufficiently stable to be considered as a robust feature of our model.

Elastic anisotropy in the mantle is commonly attributed to the preferred orientation of minerals, especially olivine crystals, in the shear strain field associated with the flow of material (e.g. Karato 1992). Our understanding of the relation between the flow pattern and the resulting elastic anisotropy has been refined by several recent studies (Chastel *et al.* 1993; Blackman *et al.* 1996; Tommasi, Vauchez & Russo 1996). Although these models show that the details of the relation between anisotropy and flow pattern may be more complex than initially intuited (Hess 1964), they confirm that the flow can produce an orientation of the olivine crystals which is compatible with the seismic observations. They show that, on the large scale at which surface waves sample the structures, the fast a axis of olivine becomes dominantly oriented in a vertical plane with the same azimuth as the flow and the maximum shear strain. For olivine crystals with their fast a axis oriented in a given direction of the horizontal plane, it is well known that the direction of the a axis determines the direction of the fast SV waves, and thereby the direction of high Rayleigh-wave phase velocity (e.g. Babuska & Cara 1991). The recent models mentioned above show that the pattern of crystal orientation is not simply horizontal and that the olivine a axis may be dominantly inclined away from the horizontal plane. Although the amplitude of Rayleigh-wave-velocity azimuthal variation gradually reduces when the a axis departs from the horizontal plane, the direction of the fastest Rayleigh wave remains in the vertical plane containing the a axis (Maupin 1984). The fast direction of horizontally propagating long-period SV waves is therefore also in this direction, and we can directly interpret our maps of fast-wave directions in terms of a axis orientation, and then in terms of the azimuth of the shear strain responsible for crystal orientation.

At lithospheric depths beneath oceans, it is commonly assumed that the flow is frozen, and that the fast-velocity direction

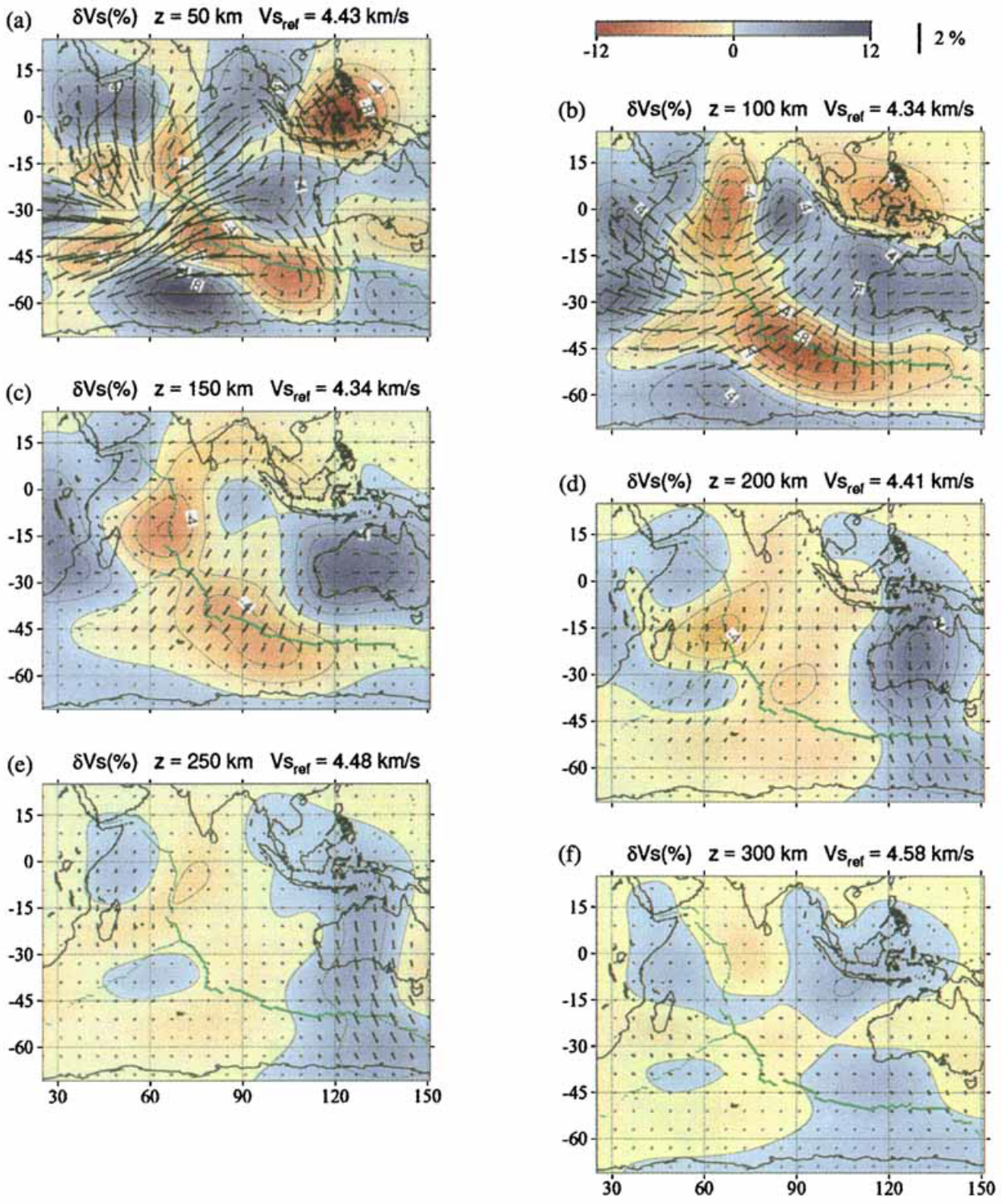

Figure 3. *SV*-velocity heterogeneities and azimuthal anisotropy at different depths. Velocity contrasts (per cent) are represented by colours; fast directions of horizontally propagating *SV* waves are represented by arrows. (a) Depth 50 km, (b) depth 100 km, (c) depth 150 km, (d) depth 200 km, (e) depth 250 km, (f) depth 300 km.

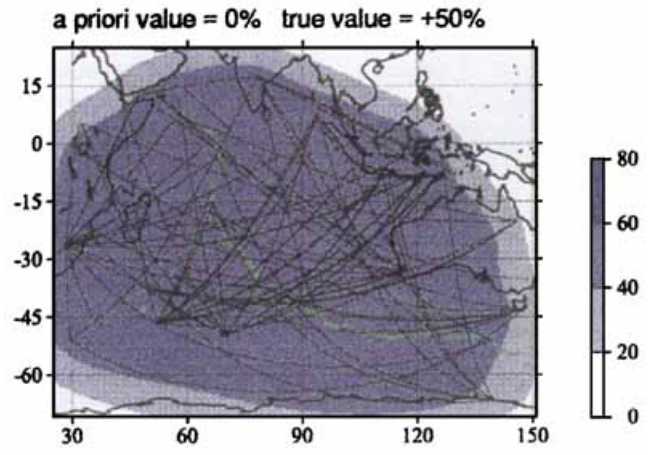

Figure 4. Synthetic experiment: recovering a flat model. Model obtained by inversion of synthetic data corresponding to a uniform +50 per cent. *S*-velocity perturbation. The synthetics have been processed using the same correlation length as for the real data (Fig. 3).

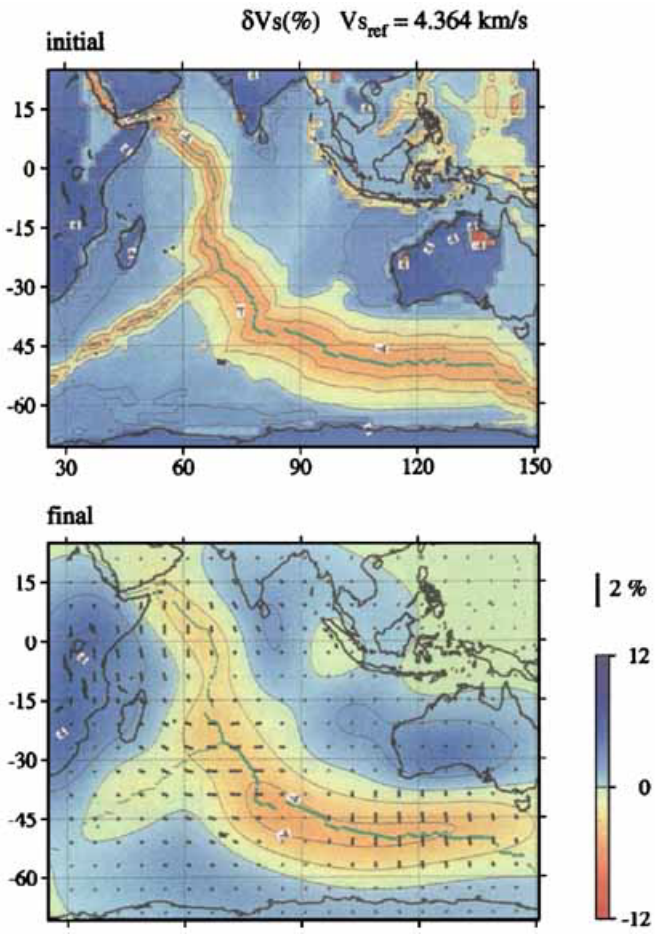

Figure 5. Synthetic experiment: recovering an isotropic-earth-like model. Model obtained by inversion of synthetic data corresponding to the *S*-velocity distribution of the 3-Smac model at 50 km depth. The displayed azimuthal anisotropy is a crude estimate of the trade-off between heterogeneities and azimuthal anisotropy.

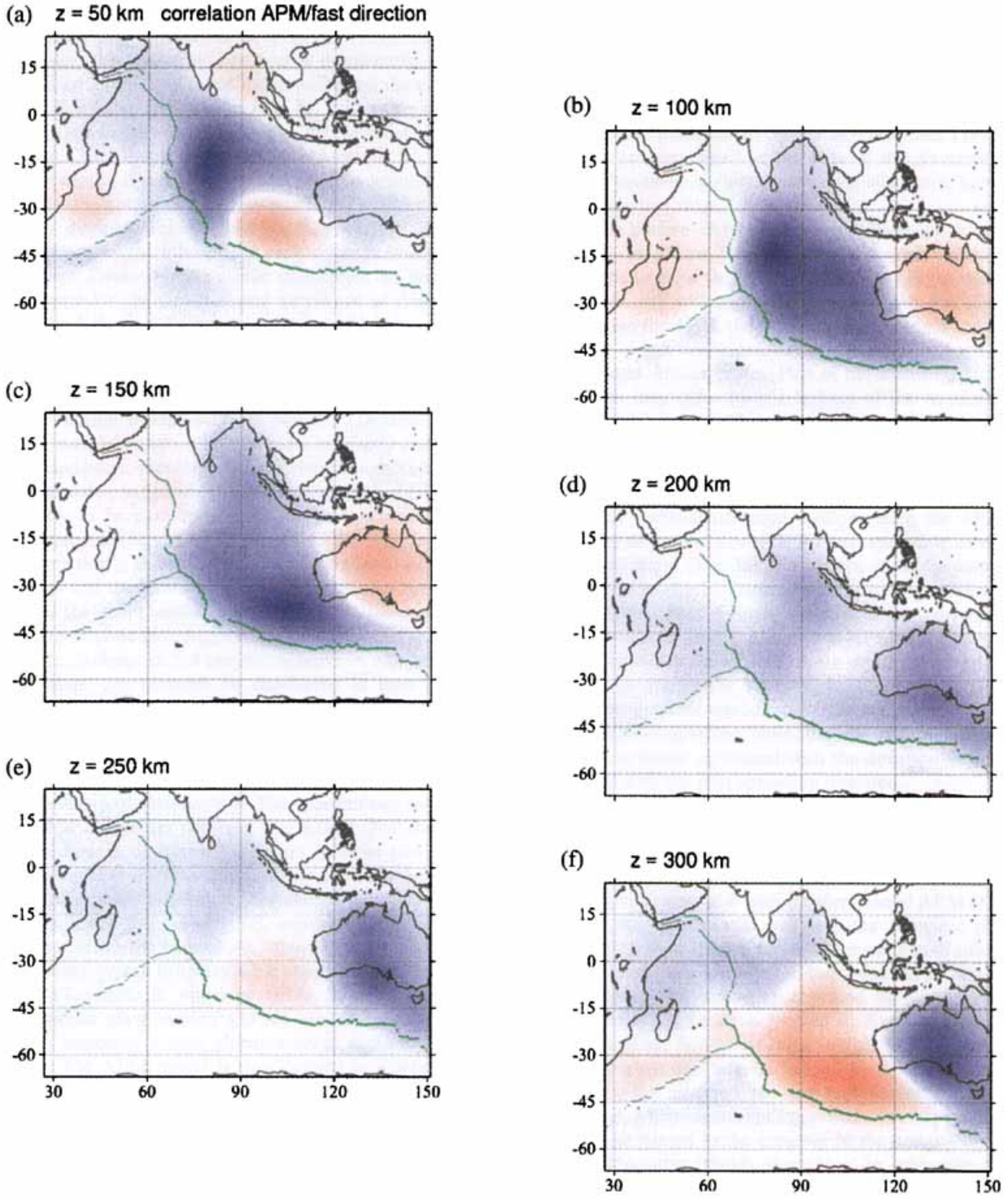

Figure 9. Correlations between fast direction of *SV* waves and plate motion direction. Good correlations (parallelism of the two vectors) are represented in blue, bad correlations (orthogonality) are represented in red. The correlation coefficient is defined as $|\overline{\text{Fast}SV}||\overline{\text{APM}}|\cos[2(\theta_{\text{Fast}SV} - \theta_{\text{APM}})]$. Note that values close to zero are obtained when the angle between the two vectors is close to 45°, but also when at least one of the two vectors is small in amplitude. The colour scales are symmetric, adapted to cover the full range of values at each depth. The amplitude of the correlation coefficient is not shown, since it depends on the anisotropy strength and is difficult to interpret.

reflects the spreading direction at which the lithosphere has been emplaced (e.g. Nishimura & Forsyth 1989). For the Indian Ocean, the spreading direction is dominantly southwest–northeast along the Central Indian ridge and the western part of the Southeast Indian ridge (Fig. 6). It is rather north–south along the Southwest Indian ridge and in older regions between the Chagos plateau and Sumatra/Australia.

At larger depths, it is more likely that the flow is not frozen, and that the orientation of the crystals reflects the direction of present-day deformation in a low-viscosity channel due to the displacement of the lithospheric plate over the underlying asthenosphere. Except for the elastic anisotropy, we have no direct evidence for the direction and amplitude of this shear strain. In the following discussion, we assume that the deformation is controlled by the differential displacement between the lithosphere and that part of the upper mantle beneath the low-viscosity layer. The lithosphere motion is robustly known from plate motion models such as Nuvel-1 (DeMets *et al.* 1990). The mantle motion is known more indirectly and with much less accuracy, essentially from global flow models. For fast-moving plates, expecially for the Pacific plate, the return flow is likely to be parallel to the plate motion and in the opposite direction (Hager & O'Connell 1979). The induced shear deformation is therefore likely to be parallel to both the plate motion and the return flow, so that it has been common to compare the sublithospheric direction of anisotropy with the direction of plate motion. In our study area, the Austral-Indian plate, moving at 7–8 cm yr^{-1} relative to the hotspot reference frame, can certainly be considered as such a fast plate, where the deformation is thus parallel to the absolute plate motion. The African and Antarctic plates are moving much more slowly. Hager & O'Connell (1979) show that for these two plates, the direction of flow may be very different from the direction of plate motion. They present two maps of modelled flow at 260 km depth in the mantle. For the two models, the flow is significantly different in these two static plates, showing that the flow direction one can infer for these regions is very model-dependent. We choose to discuss our observations using their model VII, which contains a low-viscosity channel at the base of the lithosphere and seems to provide a better overall fit to available observations of seismic anisotropy (Tanimoto & Anderson 1984). In this study, we use an absolute plate motion (APM) model derived from Nuvel-1 by imposing a null global average motion of the lithosphere. The APM model is thus defined in a way very similar to that used by Hager & O'Connell (1979), so that APM and flow are defined in a common reference frame and can be directly subtracted from one other to estimate the shear deformation. For our study area, it turns out that the predicted flow pattern is quite similar to the APM pattern (Figs 7 and 8), both in directions and amplitudes. The resulting deformation pattern should then resemble the two primary fields, and, to obtain a first rough idea, we can directly compare our fast-velocity maps to the well-constrained APM field in the whole studied area (Fig. 9).

In order to determine whether the anisotropy we observe reflects a frozen or a present-day deformation, it is important to point out in which regions of the Indian Ocean the direction of spreading, as known from the magnetic anomalies, differs most from the present day APM. In the younger regions of the Austral-Indian plate, the two directions are similar. The direction is different in the older region between the Chagos plateau and Sumatra/Australia, in the old oceanic basins west and north of Madagascar, and along the Southwest Indian ridge. A typical difference is also that the direction and speed of spreading are symmetric across a spreading ridge, whereas the shear strain may be rather discontinuous. In particular, both the flow modelled by Hager & O'Connell (1979) and the APM are very small at the base of the Antarctic plate, while the magnetic anomaly pattern is symmetric across the Southeast Indian ridge.

A simple pattern of relatively large anisotropy is obtained at a depth of 100 km (Fig. 3b). In the oceanic basins of the Austral-Indian plate, the direction of fast velocity at that depth corresponds well with the APM direction (Fig. 9b). However, in contrast to the APM, the pattern of anisotropy is continuous across the ridges and significant anisotropy is found in the Antarctic and African plates. Part of the anisotropy found in these plates may come from a leakage of the Austral-Indian plate anisotropy, due to the correlation length (1000 km) used in the tomographic inversion. However, beneath the African plate, significant anisotropy is found far from the plate boundary. The direction of this anisotropy does not correspond with the roughly north–south trend resulting from the APM and flow-model directions, nor with the past spreading direction.

At 50 km depth (Fig. 3a), the pattern is more complicated than at 100 km depth. There is a large east–west anisotropy under the West Indian ridge, which does not correlate with the direction of spreading or with the APM and flow models. Fast velocities are found in a north–south direction in the Somali basin and in the Wharton basin, in good agreement with the directions of spreading in these regions. In the eastern part of the Central Indian basin, the SW–NE direction of fast velocity is in better agreement with the direction of flow and APM than with the past spreading direction.

At 150 and 200 km depth (Figs 3c and d), the areas with a significant amount of anisotropy become more localized, and the maximum amplitude of anisotropy decreases. Under the Southeast Indian ridge at 150 km depth, the direction of anisotropy correlates well with the direction of APM (Fig. 9c), and it extends southwards well into the Antarctic plate as already observed at 100 km depth. The maximum of anisotropy is reached under the Southeast Indian ridge. At 200 km depth, the anisotropy has almost disappeared in this region, and the maximum amplitude is located in faster regions, under Australia and the Southwest Indian ridge. This could indicate that the anisotropy extends deeper in colder regions. An exception to this scheme is the slow region west of the Central Indian ridge, where significant azimuthal anisotropy still exists. This may be related to the presence of the hotspot of the La Réunion–Mauritius islands, disturbing an otherwise simpler pattern of azimuthal anisotropy. As noted in Paper I, a low-velocity region is present between 150 and 200 km depth beneath the Central Indian ridge and the hotspot of La Réunion–Mauritius. Such low velocities at these depths are consistent with recent models of mantle plumes (see Davies & Richards 1992 for a review): a plume conduit, 100 to 200 km wide horizontally, rising from the deep mantle (possibly from a thermal boundary layer at the core–mantle boundary or in the transition region), spreads out radially beneath the lithosphere, creating a hot structure near the bottom of the lithosphere. While the plume conduit may be too narrow to be seen by surface waves, the hot structure near the bottom of the lithosphere may reach 1000 km in diameter and should be

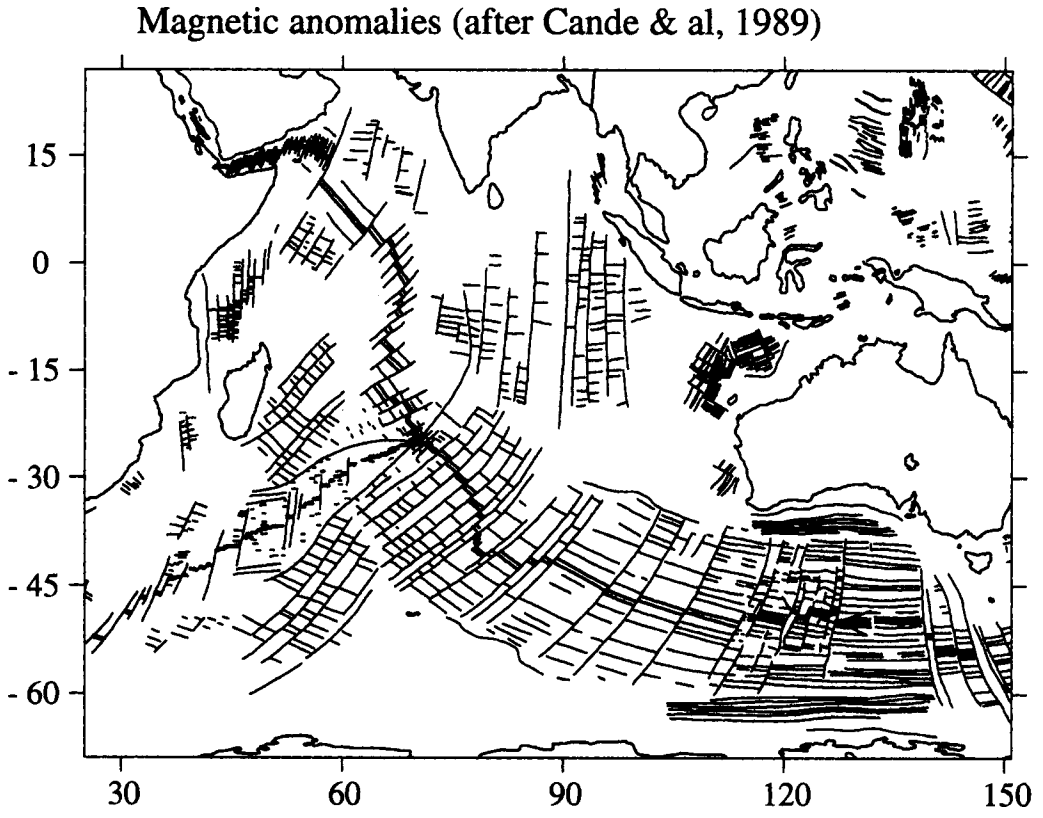

Figure 6. Magnetic anomalies in the Indian Ocean (after Cande *et al.* 1989).

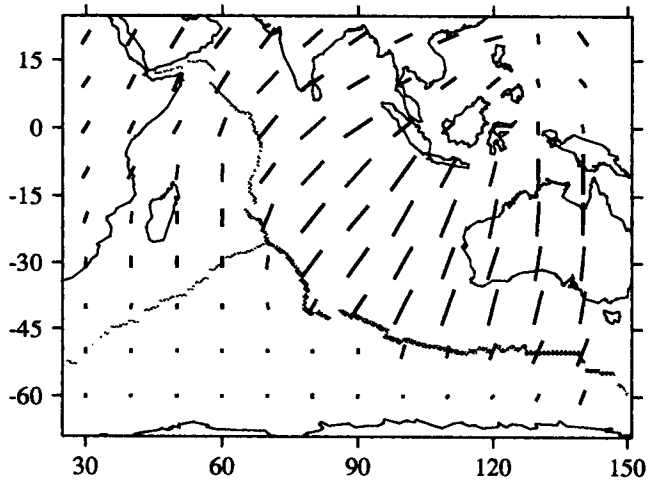

Figure 7. Mantle flow model at 260 km depth (after Hager & O'Connell 1979).

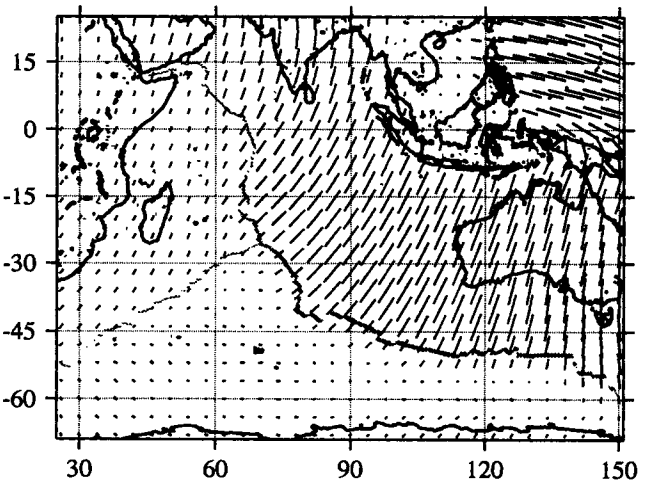

Figure 8. Absolute plate motion (APM) model derived from model Nuvel-1 (DeMets *et al.* 1990) by imposing a global null average rotation of the lithosphere.

easier to detect. A low-velocity anomaly is clearly present at 150 and 200 km depth (Figs 3c and d). How such a structure could perturb the flow pattern and the elastic anisotropy distribution remains an open question.

Another striking feature of these maps at 150 and 200 km depth can be seen beneath Australia: while anisotropy tends to be oriented east–west down to 150 km depth, it rotates to a north–south direction at 200 km depth, in agreement with the APM and the flow direction. This feature remains at greater depths (Fig. 3e). It can still be seen at 300 km depth, even though the amplitude of anisotropy becomes very small. This drastic change in the direction of anisotropy could be interpreted as an indication of the thickness of the lithosphere:

beneath Australia, the average thickness defined in this way is not likely to exceed 200 km. Below this depth, the anisotropy may reflect the northward movement of the Australian lithosphere over a low-viscosity channel, roughly 100 km thick. This observation is consistent with the depth of the anisotropic layer proposed by Leven, Jackson & Ringwood (1981) from a *P*-wave refraction profile in northern Australia. It is also supported by the previous studies of Kennett, Gudmundsson & Tong (1994) and Gudmundsson, Kennett & Goody (1994), who find, from broad-band observations in northern Australia, a high lithospheric lid, 210 km thick, overlying a low-Q zone which may be 100 or 200 km thick. Analysis of shear-wave splitting, in refracted waves returned from the upper-mantle transition zone in the same region, shows that significant polarization anisotropy is present in this asthenospheric layer (Tong, Gudmundsson & Kennett 1994). However, on the scale of the continent, high-resolution surface-wave studies (van der Hilst & Kennett 1997) suggest significant variations in the structure of the different tectonic provinces constituting the Australian continent. Moreover, this rotation of the fast direction of *S* velocity is constrained essentially by one piece of data, for the easternmost N–S path (see Fig. 1). We paid special attention to this piece of data, trying to model the related seismograms in different ways, for example with faster velocities at shallower depth. We finally found that our *S*-velocity model for this path is robust and decided to keep it in the inversion. However, there is no redundancy in our data set to constrain this feature. Further studies are therefore necessary to investigate in more detail the anisotropy of the Australian upper mantle and check whether our result is confirmed or not by new data.

Beneath Africa, no such clear indication is found. The anisotropy is weak below 100 km. The fast direction seems to rotate from NW–SE at 100 km to a quasi-N–S or NNE–SSW direction at greater depths, in quite good agreement with the direction found by Vinnik, Green & Nicolaysen (1995) from *SKS* splitting, but it is difficult to put confidence in this result, owing to the weakness of the anisotropy and, more generally, to the poor resolution we have in this region.

In Paper I, a cross-section in the velocity model shows continental roots extending down to 250–300 km. If confirmed, the anisotropy results beneath Australia presented here would support the idea of Vinnik *et al.* (1995) that deep continental roots may experience significant deformation as shallow as 200 km, due to plate motions and flow in the mantle.

6 CONCLUSIONS

We have used surface-wave and higher-mode waveform modelling to address the problem of upper-mantle anisotropy beneath the Indian Ocean, described by both radial anisotropy and the azimuthal anisotropy of *S* waves. We find a significant radial anisotropy in the uppermost 250–300 km of the mantle. The amplitude of our ξ model is smaller than what is found in global models or regional oceanic models. For azimuthal anisotropy, the situation is complex in the uppermost 100 km of the mantle. Fast-velocity directions do not correlate simply with plate motion. The similarity of fast directions to directions of fossil spreading in the Somali basin and the northern part of the Central Indian basin is in agreement with the idea of anisotropy due to frozen-in oriented crystals in the thick lithosphere of these old oceanic regions. From 100 to 200 km depth, significant correlations between the directions of fast velocities and APM appear in most oceanic regions, while no strong correlation is observed beneath continents. A relative lack of correlation shows up in the oceanic region of the La Réunion–Mauritius islands, where the pattern of anisotropy is blurred and weakened between 100 and 150 km. This complexity of the azimuthal anisotropy, together with the corresponding velocity anomaly, may be due to the presence of the hotspot.

The fast directions at 100 km depth and deeper correlate well with the direction of APM and flow for the fast-moving Austral-Indian plate, but the amplitude of anisotropy remains large under the slowly moving plates, especially under the Antarctic plate. If, as expected for slow plates, the azimuthal anisotropy reflects the flow direction and strength, our observations might indicate that a significant flow exists in the asthenosphere beneath the Antarctic plate, likely to be related to the strong upwelling at the Southeast Indian ridge. Alternatively, the azimuthal anisotropy found beneath this plate could be merely an artefact due to a leakage of the Austral-Indian plate anisotropy through the correlation length used in the inversion. A better path coverage of this region would be necessary to answer the question.

Beyond 200 km, azimuthal anisotropy vanishes beneath most of the oceanic regions, while in Australia, the directions of fast velocities correlate with plate motion down to 300 km. Deeper than 300 km, no significant correlation between anisotropy and APM is observed, and the amplitude of azimuthal anisotropy becomes negligible compared to shallower depths.

The depth extent of both azimuthal and radial anisotropy, the amplitude of radial anisotropy and the pattern of azimuthal anisotropy support the commonly accepted idea that oceanic upper-mantle anisotropy is due to the preferred orientation of olivine in the mantle. The plate motion is expected to generate an intense deformation beneath the lithosphere, thus orienting the *a* axis of olivine in the direction of maximum shear strain. From our results, this zone where anisotropy is significant and correlates in direction with present-day APM would be located at 100 to 200 km depth in oceanic areas, and at greater depths in continental areas. The deepest parts of continental roots (those parts lying below 200 km) as defined from *S*-velocity anomalies may thus be deformed by plate motions.

ACKNOWLEDGMENTS

We thank Yanick Ricard for providing us, in a numerical form, with the model of absolute plate motion derived from Nuvel-1, Marc Munschy for the plot of the magnetic anomaly map, and two anonymous reviewers for their constructive comments. Several figures have been made with the GMT software. This work has been partly funded by the CNRS under the grants 'ATP Tomographie-INSU'.

REFERENCES

Aki, K. & Kaminuma, K., 1963. Phase velocity of Love waves in Japan; Part 1: Love waves from the Aleutian shock of March 1957, *Bull. Earthq. Res. Inst.*, **41**, 243–259.

Anderson, D.L., 1966. Recent evidence concerning the structure and composition of the Earth's mantle, *Phys. Chem. Earth*, **6**, 1–131.

Babuska, V. & Cara, M., 1991. *Seismic Anisotropy in the Earth*, Kluwer Academic, Dordrecht.

Blackman, D.K., Kendall, J.M., Dawson, P.R., Wenk, H.-R., Boyce, D.

& Phipps Morgan, J., 1996. Teleseismic imaging of subaxial flow at mid-ocean ridges: traveltime effects of anisotropic mineral texture in the mantle, *Geophys. J. Int.*, **127,** 415–426.

Cande, S.C., LaBrecque, J.L., Larson, R.L., Pitman, W.C., III, Golovchenko, X. & Haxby, W.F., 1989. *Magnetic Lineations of the World's Ocean Basins,* map, American Association of Petroleum Geologists, Tulsa.

Cara, M. & Lévêque, J.-J., 1987. Waveform inversion using secondary observables, *Geophys. Res. Lett.*, **14,** 1046–1049.

Cara, M. & Lévêque, J.-J., 1988. Anisotropy of the asthenosphere: the higher mode data of the Pacific revisited, *Geophys. Res. Lett.*, **15,** 205–220.

Chastel, Y.B., Dawson, P.R., Wenk, H.-R. & Bennett, K., 1993. Anisotropic convection with implications for the upper mantle, *J. geophys. Res.*, **98,** 17 757–17 771.

Christensen, N.I. & Salisbury, M.H., 1979. Seismic anisotropy in the oceanic upper mantle: evidence from the Bay Islands Ophiolite Complex, *J. geophys. Res.*, **84,** 4601–4610.

Crampin, S., 1981. A review of wave motion in anisotropic and cracked elastic media, *Wave Motion,* **3,** 343–391.

Crampin, S., 1984. An introduction to wave propagation in anisotropic media, *Geophys. J. R. astr. Soc.*, **76,** 17–28.

Davies, G.F. & Richards, M.A., 1992. Mantle convection, *J. Geol.*, **100,** 151–206.

Debayle, E., 1996. Tomographie du manteau supérieur de l'Océan Indien par inversion de forme d'ondes, *Thèse de Doctorat,* Université Louis Pasteur, Strasbourg.

Debayle, E. & Lévêque, J.-J., 1997. Upper mantle heterogeneities in the Indian Ocean from waveform inversion, *Geophys. Res. Lett.*, **24,** 245–248.

DeMets, C., Gordon, R.G., Argus, D.F. & Stein, S., 1990. Current plate motions, *Geophys. J. Int.*, **101,** 425–478.

Dziewonski, A.M. & Anderson, D.L., 1981. Preliminary reference Earth model, *Phys. Earth planet. Inter.*, **25,** 297–356.

Estey, L.H. & Douglas, B.J., 1986. Upper mantle anisotropy: a preliminary model, *J. geophys. Res.*, **91,** 11 393–11 406.

Forsyth, D.W., 1975. The early structural evolution and anisotropy of the oceanic upper mantle, *Geophys. J. R. astr. Soc.*, **43,** 103–162.

Gudmundsson, O., Kennett, B.L.N. & Goody, A., 1994. Broadband observations of upper-mantle seismic phases in northern Australia and the attenuation structure in the upper mantle, *Phys. Earth planet. Inter.*, **84,** 207–226.

Hadiouche, O., Jobert, N. & Montagner, J.-P., 1989. Anisotropy of the African continent inferred from surface waves, *Phys. Earth planet. Inter.*, **58,** 61–81.

Hager, H.H. & O'Connell, R.J., 1979. Kinematic models of large-scale flow in the Earth's mantle, *J. geophys. Res.*, **84,** 1031–1048.

Hess, H.H., 1964. Seismic anisotropy of the upper mantle under oceans, *Nature,* **203,** 629–631.

Jech, J. & Psencik, J., 1989. First-order perturbation method for anisotropic media, *Geophys. J. Int.*, **99,** 369–376.

Karato, S., 1992. On the Lehmann discontinuity, *Geophys. Res. Lett.*, **19,** 2255–2258.

Kawasaki, I. & Konno'o, F., 1984. Azimuthal anisotropy of surface waves and the possible type of seismic anisotropy due to preferred orientation of olivine in the uppermost mantle beneath the Pacific Ocean, *J. Phys. Earth,* **32,** 229–244.

Kennett, B.L.N., Gudmundsson, O. & Tong, C., 1994. The upper-mantle S and P velocity structure beneath northern Australia from broad-band observations, *Phys. Earth planet. Inter.*, **86,** 85–98.

Leven, J.H., Jackson, I. & Ringwood, A.E., 1981. Upper mantle seismic anisotropy and lithospheric decoupling, *Nature,* **289,** 234–239.

Lévêque, J.-J., Cara, M. & Rouland, D., 1991. Waveform inversion of surface wave data: test of a new tool for systematic investigation of upper mantle structures, *Geophys. J. Int.*, **104,** 565–581.

Maupin, V., 1984. Modélisation d'ondes de surface en milieu anisotrope à symétrie axiale, *Diplôme d'Ingénieur, Géophysicien,* Université Louis Pasteur, Strasbourg.

Maupin, V. & Cara, M., 1992. Love–Rayleigh wave incompatibility and possible deep upper mantle anisotropy in the Iberian peninsula, *Pageoph,* **138,** 429–444.

Mochizuki, E., 1986. The free oscillations of an anisotropic and heterogeneous earth, *Geophys. J. R. astr. Soc.*, **86,** 167–176.

Montagner, J.-P., 1986. Regional three-dimensional structures using long-period surface waves, *Ann. Geophys.*, **4,** 283–294.

Montagner, J.-P. & Jobert, N., 1988. Vectorial tomography, 2. Application to the Indian Ocean, *Geophys. J. R. astr. Soc.*, **94,** 309–344.

Montagner, J.-P. & Nataf, H.-C., 1986. A simple method for inverting the azimuthal anisotropy of surface waves, *J. geophys. Res.*, **91,** 511–520.

Montagner, J.-P. & Kennett, B.L.N., 1996. How to reconcile body-wave and normal-mode reference earth models, *Geophys. J. Int.*, **125,** 229–248.

Montagner, J.-P. & Tanimoto, T., 1990. Global anisotropy in the upper mantle inferred from the regionalization of phase velocities, *J. geophys. Res.*, **95,** 4797–4819.

Montagner, J.-P. & Tanimoto, T., 1991. Global upper mantle tomography of seismic velocities and anisotropies, *J. geophys. Res.*, **96,** 20 337–20 351.

Nataf, H.-C. & Ricard, Y., 1995. 3SMAC: an a priori tomographic model of the upper mantle based on geophysical modeling, *Phys. Earth planet. Inter.*, **95,** 101–122.

Nataf, H.-C., Nakanishi, I. & Anderson, D.L., 1984. Anisotropy and shear-velocity heterogeneities in the upper mantle, *Geophys. Res. Lett.*, **11,** 109–112.

Nishimura, C.E. & Forsyth, D.W., 1989. The anisotropic structure of the upper mantle in the Pacific, *Geophys. J.*, **96,** 203–229.

Nolet, G., 1990. Partitioned waveform inversion and two-dimensional structure under the network of autonomously recording seismographs. *J. geophys. Res.*, **95,** 8499–8512.

Peselnick, L. & Nicolas, A., 1978. Seismic anisotropy in an ophiolite peridotite: application to oceanic upper mantle, *J. geophys. Res.*, **83,** 1227–1235.

Roult, G., Rouland, D. & Montagner, J.-P., 1987. Velocity distribution in the Indian Ocean and Indonesian region inferred from Geoscope records, *Geophys. Res. Lett.*, **14,** 343–346.

Smith, M.L. & Dahlen, F.A., 1973. The azimuthal dependence of Love and Rayleigh wave propagation in a slightly anisotropic medium, *J. geophys. Res.*, **78,** 3321–3333.

Takeuchi, H. & Saito, M., 1972. Seismic surface waves, in *Methods in Computational Physics,* Vol. 11, pp. 217–295, Academic Press, London.

Tanimoto, T., 1986a. The Backus–Gilbert approach to the 3-D structure in the upper mantle—II. SH and SV velocity, *Geophys. J. R. astr. Soc.*, **84,** 49–69.

Tanimoto, T., 1986b. Free oscillations of a slightly anisotropic Earth, *Geophys. J. R. astr. Soc.*, **87,** 493–517.

Tanimoto, T. & Anderson, D.L., 1984. Mapping convection in the mantle, *Geophys. Res. Lett.*, **11,** 287–290.

Tanimoto, T. & Anderson, D.L., 1985. Lateral heterogeneity and azimuthal anisotropy of the upper mantle: Love and Rayleigh waves 100–250 sec, *J. geophys. Res.*, **90,** 1842–1858.

Tong, C., Gudmundsson, O. & Kennett, B.L.N., 1994. Shear wave splitting in refracted waves returned from the upper mantle transition zone beneath northern Australia, *J. geophys. Res.*, **99,** 15 783–15 797.

Tommasi, A., Vauchez, A. & Russo, R., 1996. Seismic anisotropy in ocean basins: resistive drag of the sublithospheric mantle?, *Geophys. Res. Lett.*, **23,** 2991–2994.

van der Hilst, R.D. & Kennett, B.L.N., 1997. Upper mantle structure beneath Australia from portable array deployments, in *The Structure and Dynamics of the Australian Lithosphere,* eds Braun, J., Dooley, J. & Klootwijk, C., *Am. geophys. Un. Monogr.*, submitted.

Vinnik, L.P., Green, R.W.E. & Nicolaysen, L.O., 1995. Recent deformations of the deep continental root beneath southern Africa, *Nature,* **375,** 50–52.

APPENDIX A: VELOCITY OF HORIZONTALLY PROPAGATING LONG-PERIOD *SH* AND *SV* WAVES IN ANISOTROPIC STRUCTURES

As already noticed by Montagner & Nataf (1986), the combinations of elastic coefficients $\hat{L}$ and $\hat{N}$, controlling the dominant first-order variations of surface-wave phase velocities in anisotropic structures, control also the velocities of horizontally propagating *SV* and *SH* waves in a weakly anisotropic medium having a horizontal symmetry plane (Crampin 1981). The expressions obtained for the first-order variations of the surface-wave phase velocities are valid in fully anisotropic structures. On the other hand, up to now, the equivalence to perturbation of body-wave velocities has been shown only for media having a horizontal symmetry plane, where the two quasi-*S* waves are polarized as *SV* and *SH*. We show in this Appendix that the restriction to models having a horizontal symmetry plane is not necessary, and that the same interpretation of $\hat{L}$ and $\hat{N}$ in terms of velocities of *SV* and *SH* waves is possible in fully anisotropic structures. We suppose here that the anisotropy is weak, and can be considered as a small perturbation to a reference isotropic structure.

The apparent velocity of long-period *S* waves

In a fully anisotropic medium, the polarizations of the two quasi-*S* waves propagating horizontally are usually not *SV* and *SH*. We have therefore to define what we mean by the apparent velocity of *SV* or *SH* waves in fully anisotropic structures.

It is well known that long-period *SKS* waves, having travelled through an anisotropic upper mantle, although having a transverse component which is much studied, are still polarized dominantly along the radial direction. More generally, *S* waves dominantly keep their initial polarization when traversing an anisotropic region, if their dominant periods are much larger than the time difference for propagation of the fast and slow *S* waves in the anisotropic zone. Let us note that there is a trade-off in this approximation between the periods which can be considered, the strength of the anisotropy and the distance of propagation. Provided the anisotropy is sufficiently weak, this approximation is valid for any period and propagation distance. We define the apparent velocity of a long-period *S* wave with a given initial polarization as the velocity measured for the dominant component, along the initial polarization direction. Let us first find the general expression for this apparent velocity, after propagation in a weakly anisotropic homogeneous region.

In such a medium, the three body waves propagating in a given direction can be separated into a quasi-*P* wave and two quasi-*S* waves. The two quasi-*S* waves, S_1 and S_2, propagate at two different velocities. They are dominantly polarized in the plane perpendicular to the propagation direction, as is the initial *S* wave. In this plane, we define an orthogonal coordinate frame $(\mathbf{e}_1, \mathbf{e}_2)$ such that the displacement of the initial *S* wave is along $\mathbf{e}_1$. The polarization of S_1 then makes an angle α with that direction. When entering the anisotropic region, the initial *S* wave is split into the two quasi-*S* waves S_1 and S_2. For a harmonic displacement of the initial *S* wave equal to

$$\mathbf{u} = \begin{pmatrix} \exp[i\omega(t - t_0)] \\ 0 \end{pmatrix}, \tag{A1}$$

the displacement after propagation for a distance l in the anisotropic region is equal to

$$\mathbf{u} = \cos\alpha \begin{pmatrix} \cos\alpha \exp\{i\omega[t - t_0 - l/(v_0 + \delta v_1)]\} \\ \sin\alpha \exp\{i\omega[t - t_0 - l/(v_0 + \delta v_1)]\} \end{pmatrix} + \sin\alpha \begin{pmatrix} \sin\alpha \exp\{i\omega[t - t_0 - l/(v_0 + \delta v_2)]\} \\ -\cos\alpha \exp\{i\omega[t - t_0 - l/(v_0 + \delta v_2)]\} \end{pmatrix}, \tag{A2}$$

where $v_0 + \delta v_1$ and $v_0 + \delta v_2$ are the velocities of the S_1 and S_2 waves respectively, and v_0 is the velocity of the *S* wave in the reference isotropic structure, which is chosen close to the anisotropic structure. In the approximation that $\omega l \delta v_i / v_0^2$ is small, a series of expansions, where we keep zero- and first-order terms only, can be made. Eq. (A2) becomes

$$\mathbf{u} = \begin{pmatrix} \exp\left[i\omega\left(t - t_0 - \dfrac{l}{v_0 + \delta v_1 \cos^2\alpha + \delta v_2 \sin^2\alpha}\right)\right] \\ 2i\omega \cos\alpha \sin\alpha \dfrac{1}{v_0^2}(\delta v_1 - \delta v_2) \exp\left[i\omega\left(t - t_0 - \dfrac{l}{v_0}\right)\right] \end{pmatrix}. \tag{A3}$$

The displacement along the dominant component is equal to the initial displacement propagating at an apparent velocity $v_0 + \delta v_1 \cos^2\alpha + \delta v_2 \sin^2\alpha$.

The velocity as a function of the elastic parameters

Let us now express this apparent velocity as a function of the elements of the elastic tensor in the anisotropic structure. The first-order polarizations and velocities of body waves in weakly anisotropic structures, calculated using perturbation theory, are given by Jech & Psencik (1989). These authors give, in the same notation as above,

$$\delta v_1 = \frac{1}{4v_0}(B_{11} + B_{22} + \sqrt{\Delta}),$$

$$\delta v_2 = \frac{1}{4v_0}(B_{11} + B_{22} - \sqrt{\Delta}),$$

$$\cos^2\alpha = \frac{1}{2}[1 + (B_{11} - B_{22})/\sqrt{\Delta}], \tag{A4}$$

with

$$\Delta = (B_{11} - B_{22})^2 + 4B_{12}^2,$$

$$B_{mm} = \frac{1}{\rho}\Delta C_{ijkl} n_i n_l e_j^{(m)} e_k^{(n)}.$$

Here ρ is the density, ΔC is the difference between the elastic tensors in the anisotropic and isotropic reference structures, $\mathbf{n}$ is a unit vector in the propagation direction and $(\mathbf{e}^{(m)}, \mathbf{e}^{(n)})$ are two unit vectors perpendicular to each other in the *S*-wave polarization plane. Here we take these two vectors as equal to the $\mathbf{e}_1$ and $\mathbf{e}_2$ defined in the previous section.

Combining these elements with the expression $\delta v = \delta v_1 \cos^2\alpha + \delta v_2 \sin^2\alpha$ for the velocity perturbation of the

long-period S wave polarized initially along $\mathbf{e}_1$, we obtain

$$\delta v = \frac{B_{11}}{2v_0}. \tag{A5}$$

Velocities of *SH* and *SV* waves propagating horizontally

For S waves propagating horizontally in the azimuth θ, we have $\mathbf{n} = (\cos\theta, \sin\theta, 0)$, $\mathbf{e}_1 = (-\sin\theta, \cos\theta, 0)$ for SH waves and $\mathbf{e}_1 = (0, 0, 1)$ for SV waves. Substituting in eq. (A5), and using the notation of Montagner & Nataf (1986), modified from Crampin (1984), for the elements of the elastic tensor, we obtain the velocity perturbations for the two kinds of waves:

$$\delta v_{SH} = \frac{1}{2v\rho}(N - N_{\text{iso}} - C_{\text{C}}\cos 4\theta - C_{\text{S}}\sin 4\theta) = \frac{1}{2v\rho}(\hat{N} - N_{\text{iso}}) \tag{A6}$$

and

$$\delta v_{SV} = \frac{1}{2v\rho}(L - L_{\text{iso}} + G_{\text{C}}\cos 2\theta + G_{\text{S}}\sin 2\theta) = \frac{1}{2v\rho}(\hat{L} - L_{\text{iso}}). \tag{A7}$$

The combinations of elastic parameters controlling the velocity of horizontally propagating long-period SH and SV waves are $\hat{N}$ and $\hat{L}$, the same as those having the dominant influence on the phase velocity of Love and Rayleigh waves respectively. The average elastic models, as a function of depth, that we obtain from the waveform inversion thus have a simple interpretation in terms of the velocities of horizontally propagating body waves, or their ratios, even in fully (but weakly) anisotropic models.